## Material Scaling and Frequency-Selective Enhancement of Near-Field Radiative Heat Transfer for Lossy Metals in Two Dimensions via Inverse Design

Weiliang Jin,<sup>1</sup> Sean Molesky,<sup>1</sup> Zin Lin,<sup>2</sup> and Alejandro W. Rodriguez<sup>1</sup>

<sup>1</sup>Department of Electrical Engineering, Princeton University, Princeton, NJ, 08544 <sup>2</sup>John A. Paulson School of Engineering and Applied Sciences Harvard University, Cambridge, MA, 02138

The super-Planckian features of radiative heat transfer in the near-field are known to depend strongly on both material and geometric design properties. However, the relative importance and interplay of these two facets, and the degree to which they can be used to ultimately control energy flow, remains an open question. Recently derived bounds suggest that enhancements as large as  $|\chi|^4 \lambda^2 / \left((4\pi)^2 \operatorname{Im}\left[\chi\right]^2 d^2\right)$  are possible between extended structures (compared to blackbody); but neither geometries reaching this bound, nor designs revealing the predicted material  $(\chi)$  scaling, have been previously reported. Here, exploiting inverse techniques, in combination with fast computational approaches enabled by the low-rank properties of elliptic operators for disjoint bodies, we investigate this relation between material and geometry on an enlarged space structures. Crucially, we find that the material proportionality given above does indeed emerge in realistic structures. In reaching this result, we also show that (in two dimensions) lossy metals such as tungsten, typically considered to be poor candidate materials for strongly enhancing heat transfer in the near infrared, can be structured to selectively realize flux rates that come within 50% of those exhibited by an ideal pair of resonant lossless metals for separations as small as 2% of a tunable design wavelength.

Radiative heat transfer (RHT) between objects separated by near-field distances (on the order or shorter than the thermal wavelength) exhibits a number of remarkable features. Primarily, evanescent contributions, absent in the far-field, cause the rate of heat exchange to scale inversely with separation down to nanometer scales, leading to flux rates many orders of magnitude larger than those predicted by the Stefan-Boltzmann (blackbody) law [1–4]. Further, this increased flux can be enhanced and controlled by resonant electromagnetic surface modes [5–8], allowing heat to be concentrated into narrow and designable spectral bandwidths. These properties, in principle, provide a means of significantly improving the degree to which heat can be manipulated compared to thermal conduction, leading to the consideration of applications and devices based on near-field RHT in various contexts, with proposals ranging from thermophotovoltaics energy capture [9– 14] to high-density heat management [15–17], and heat assisted magnetic recording [18, 19].

Yet, a concrete understanding of what can be accomplished with near-field RHT remains elusive. Simple high-symmetry structures where analytic solutions are possible provide valuable insight, but appear to be far from ideal. In particular, the most well-studied platform for implementing selective RHT enhancement [20, 21], involving parallel metal plates [22-25] supporting surface resonances (plasmon or phonon polaritons) [26, 27], has critical deficiencies. First, as dictated by the Planck distribution, there is a natural wavelength scale for observing significant thermal radiative effects near ambient temperatures that spans the near to mid infrared (1 to 10  $\mu$ m) spectrum [28-30]. Typical (low-loss) optical materials do not support polariton resonances at these wavelengths, and often lack sufficient thermal stability to withstand longterm operation [31-33]. Second, the tightest known limits of RHT between extended structures, recently derived using energy conservation and reciprocity arguments [34], reveal that both practical material ( $|\chi|^2/\text{Im}\,\chi$ ) and geometric ( $\lambda/d$ ) factors

seemingly enable enhancements relative to blackbody emission as large as

$$\mathcal{F}_{\text{limit}} \le \left(\frac{1}{4\pi} \frac{\lambda}{d} \frac{|\chi|^2}{\text{Im}[\chi]}\right)^2,\tag{1}$$

orders of magnitude larger than what is achievable with ideal planar media, suggesting that dramatic improvements are possible through the use of nanostructured surfaces [34]. (In this expression, d stands for separation, and  $\chi$  material susceptibility, assumed to be the same in both bodies.) Moreover, the  $|\chi|^4/\text{Im}\left[\chi\right]^2$  scaling in (1) indicates that materials exhibiting strong metallic response, far from the typical planar surface-plasmon polariton (SPP) condition  $\text{Re}\left[\chi\right]=-2$ , have much greater potential for enhancement. To date, however, this behaviour has not been observed, and tested geometries employing non-resonant materials [35–39] have yet to surpass the optimal rates associated with planar bodies.

In this article, we provide direct evidence of this material scaling enhancement in periodic systems. Building on our earlier examination of RHT between multilayer bodies [40], we now employ inverse design [41] to investigate RHT between generalized two-dimensional gratings (restricting the analysis to realistic materials and fabricable structures). Focusing on lossy metals far from the SPP condition at infrared wavelengths, we observe that while  $\mathcal{F}$  does not approach (1), the predicted material scaling is nevertheless present. For the specific example of tungsten (W), we also find a grating geometry that selectively achieves 50% of the RHT of a pair of ideal, lossless metal plates satisfying the SPP condition, for separations as small as 2% of a tunable design wavelength. These predictions represent RHT enhancements of nearly two orders of magnitude compared to corresponding planar objects, confirming the potential of even relatively simple structuring for selectively enhancing RHT.

The application of inverse design to selective RHT enhancement between extended structures is complicated in sev-

eral ways. First, near-field RHT is controlled by evanescent electromagnetic fluctuations. The large density of these states makes it challenging to apply traditional resonant nanophotonic strategies for enhancing far-field emission over narrow spectral windows [42, 43]. Moreover, the characteristically large field amplitudes and sub-wavelength features of evanescent states make them sensitive to small variations in structural and material properties [44], and correspondingly accurate modeling of RHT requires fine numerical resolution [45-48].) Second, unlike the far field, RHT can not be decomposed into approximately equivalent independent subproblems. Alterations in the structure of any one object affects the response of the entire system, meaning that the scattering properties of all bodies must be controlled simultaneously. Finally, Maxwell's equations depend nonlinearly on the dielectric properties and shapes of all bodies, making the optimization non-convex [49] and any a priori guarantee of globally optimal solutions impossible.

Consequently, tractable general approaches for simply calculating near-field RHT have only recently been realized [45– 47, 50], and nearly all previously studied geometries have been designed via trial-and-error approaches exploiting bruteforce search over a handful of high-symmetry design parameters [51]. Beginning with bulk metamaterials [39, 52–57], thin films [58-62], plasmonic materials [50, 55, 62-64], and more recently, metallic metasurfaces [35, 65, 66] and gratings [38, 64, 67–69], selective RHT enhancement has primarily been achieved by tuning the permittivity response, either real or effective, to create or mimic surface resonances [70]. (Notably, a recent silicon metasurface design [35] was predicted to have a larger integrated RHT than planar SiO<sub>2</sub>, which exhibits low-loss surface phonon polaritons, down to gap distances of 10 nm.) Other similarly high symmetry approaches have sought to increase the photonic density of states by exploiting interference (hybridization [71]) among the localized plasmons of individual nanostrutures [72]. Building from simple shapes, tunable RHT rates have been demonstrated in nanobeam (triangluar, ellipsoidal, and rectangular unit cells) and nanoantenna arrays exploiting both Mie [73] and Fano [74, 75] resonances. Although conceptually promising, these approaches have been found to have diminishing returns at small separations (relative to the thermal wavelength).

In the case of periodic gratings, RHT is

$$\Phi(\omega) = \frac{1}{2\pi} \int \frac{\mathrm{d}^n \mathbf{k}}{(2\pi)^n} \, \mathcal{T}(\omega, \mathbf{k}), \qquad (2)$$

where the integration is carried out over Bloch-vectors  $\mathbf{k}$  in the first Brillouin zone (BZ), and the scattering properties of the structures are captured by the transfer function  $\mathcal{T}(\omega,\mathbf{k})$  described by (6). To maximize the transfer function, both the density and coupling efficiency of the participating states [76, 77] must be made as large as possible at all  $\mathbf{k}$ . A similar problem arises in the design of far-field emitters [44, 78–82], where resonant structures are often intuitively designed to match the absorption and coupling rates of a wide range of externally excited states, leading to a com-

plete suppression of scattered fields. But the task here is more complicated, as the electromagnetic field must be regulated over a much larger (evanescently coupled) range. For intuition based structures with a few tunable parameters, there does not seem to be enough design freedom to reach this level of control, with the range of rate-matched states occurring in current designs [36] falling short of those achievable in planar high index dielectrics (n > 3). Without a viable means of addressing these questions, we turn to inverse techniques [41].

As an initial step towards the broader development of this area, and for computational convenience, we focus exclusively on two-dimensional gratings. This choice has major consequences for the underlying physical processes. Particularly, in moving from three to two dimensions, the geometric and material scaling of the density of states decreases and as a result, the maximum RHT rate between two ideal planar metals,  $\operatorname{Re}\left[\chi\left(\omega\right)\right]=-2$ , becomes finite in the limit of vanishing loss [341,

$$\mathcal{F}_{\rm pl}^{2D}\left(\omega\right) = \frac{1}{2\pi} \frac{\lambda}{d},\tag{3}$$

 $\mathcal{F}(\omega)=\Phi(\omega)/\Phi_0(\omega),$  and  $\Phi_0(\omega)=\omega/\pi^2c~(\omega^2/4\pi^2c^2)$  the spectral emission rate per unit area of a two (three) dimensional planar blackbody. In contrast,  $\mathcal{F}^{3D}_{\rm pl}(\omega)=\lambda^2\ln\left(2/{\rm Im}[\chi(\omega)]\right)/\left(2\pi^2d^2\right)$  exhibits stronger geometric and material enhancement factors. Consequently, achieving a strong material response  $\chi\left(\omega\right)$  at the desired frequency window along with broadband rate-matching through nanostructuring is expected to have more significant impact in three dimensions. As (3) is useful standard for comparing the efficacy of any given design it will be used as a normalization throughout the remainder of the manuscript.

Keeping these considerations in mind, we now describe a computational method that allows fast computations of RHT between arbitrarily shaped gratings of period  $\Lambda$ , separated by a vacuum gap d. Within fluctuational electrodynamics, the calculation of RHT consist of determining the absorbed power within a body B,  $\Phi(\omega) = \frac{1}{2}\omega\varepsilon_o\int_{V_B}d\mathbf{r}'$  Im  $[\chi(\mathbf{r}',\omega)]$   $\langle |\mathbf{E}(\mathbf{r}',\omega)|^2 \rangle$ , resulting from thermally excited current sources originating within a different body A. Given a discretized computational grid and assuming local media, these sources obey the fluctuation—dissipation relation [83],

$$\langle j_{\gamma,i}^* j_{\beta,j} \rangle = \frac{4\omega\epsilon_o}{\pi} \delta_{ij} \delta_{\gamma\beta} \operatorname{Im}[\chi_i(\omega)] \Theta(\omega, T_i).$$
 (4)

Here,  $\Theta(\omega,T)=\hbar\omega/(\mathrm{e}^{\hbar\omega/k_BT}-1)$  is the Planck function,  $\langle\ldots\rangle$  a thermal ensemble average,  $\{i,j\}$  the index of a given location or pixel within the computational grid, and  $\{\gamma,\beta\}=\{x,y,z\}$  the vector polarizations. Equation (4) can be used in conjunction with knowledge of the electric Green's function  $\mathcal G$  of the system [84], to obtain,

$$\Phi(\omega) = \frac{\omega^4 \Theta(\omega, T)}{2\pi c^4} \sum_{\beta, \gamma} \int_{V_A} d\mathbf{r} \int_{V_B} d\mathbf{r}'$$

$$\operatorname{Im} \left[ \chi(\mathbf{r}, \omega) \right] \operatorname{Im} \left[ \chi(\mathbf{r}', \omega) \right] \left| \mathcal{G}_{\beta\gamma}(\mathbf{r}', \mathbf{r}, \omega) \right|^2. \tag{5}$$

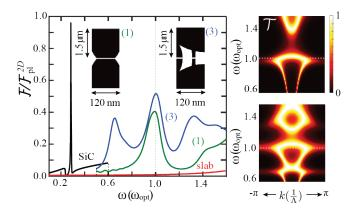


FIG. 1. Inverse design of selective near-field heat transfer between periodic tungsten gratings: Near-field RHT enhancement for inverse-designed tungsten gratings  $\mathcal{F}$ , along with that of planar silicon carbide for comparison, relative to the enhancement achieved with ideal (lossless) planar metals,  $\mathcal{F}_{pl}^{2D}$  given in (3), with respect to frequency  $\omega$  (left). Profiles of the structures are displayed as insets. Color plots depicting the k-dependent transfer functions  $\mathcal{T}(\omega, \mathbf{k})$  over the chosen frequency range are shown on the right. The depicted optimization proceeds from an unstructured planar system (0) to structured gratings (N) by successively introducing additional ellipsoidal degrees of freedom "N" to the design space. Performance is qualified by the magnitude of RHT at a single design frequency  $\omega_{\rm opt} = 2\pi c/3 \ \mu {\rm m} \ (\lambda_{\rm opt} = 3 \ \mu {\rm m})$ , where tungsten behaves as a highly lossy metal far from the planar surface plasmon resonance. The gap separation and the period of gratings are  $d(\Lambda) = 0.02 \ (0.04) \ \lambda_{\rm opt}$ , respectively. Even in the case of a single ellipsoid, producing a relative simple grating, heat transfer is enhanced by a factor of 40, while the more complicated design (3) is observed to come within 50% of the ideal planar limit.

Writing this in matrix form, with superscripts denoting projections onto the respective body, and  $\mathcal{G}$  denoting the matrix form of the electric Green's function, it follows that RHT can be written as a Frobenius norm,

$$\Phi\left(\omega\right) = \frac{\omega^4 \Theta\left(\omega, T\right)}{2\pi c^4} \left| \left| \sqrt{\operatorname{Im}\left[\chi^A\right]} \mathcal{G}^{AB} \sqrt{\operatorname{Im}\left[\chi^B\right]} \right| \right|_F^2. \quad (6)$$

The main challenge in evaluating (6) lies in the need to repeatedly evaluate and multiply  $\mathcal{G}^{AB}$ , the inverse of a sparse matrix. Direct application of either sparse-direct [85] or iterative solvers [86] would demand extraordinary computational resources, especially in three dimensions. In particular, without additional simplifications, within a particular numerical discretization, the number of computations at each iteration of an optimization required is at least the rank of the matrix  $\sqrt{\text{Im}\left[\chi^{B}\right]}$ , or three times the number pixels in B (polarizations). However, because  $\mathcal{G}^{AB}$  does not describe fields created by current sources within the same body (but only disjoint bodies), it admits a low-rank approximation [87]. Hence, (6) can be well approximated by a singular value decomposition of the matrix  $\mathcal{Z}^{AB} = \sqrt{\text{Im}\left[\chi^{A}\right]}\mathcal{G}^{AB}\sqrt{\text{Im}\left[\chi^{B}\right]}$ ,

$$\Phi(\omega) = \frac{\omega^4 \Theta(\omega, T)}{2\pi c^4} \sum_{i} |\sigma_i|^2, \tag{7}$$

requiring only a small set of singular values  $\{\sigma_i\}$ . Applying the fast randomized SVD algorithm [88], detailed in Appendix A, we find that typically no more than 8 singular values are needed to reach an error estimate better than  $1 \cdot 10^{-3}$ , reducing the number of required matrix solves to  $\lesssim 16$ . (As derived in Appendix B, this trace formulation also enables fast gradient computations via the adjoint method [41].)

The inverse problem is then to maximize  $\sum_{i} |\sigma_{i}|^{2}$  with respect to variations in  $\chi$ . Such an optimization can be carried out in the framework of topology optimization using the adjoint method [41], allowing a huge range of design parameters (each pixel within the optimization domain). We find, however, that local, gradient-based optimization leads to slow convergence to fabricable structures and comparatively suboptimal designs. To avoid these difficulties, we instead considered a range of shape optimizations [41]. While limiting the space of discoverable structures, this choice allows for application of statistical Bayesian algorithms [89, 90] in combination with fast, gradient-based optimization. Specifically, the susceptibility profile over the periodic computational domain is described by the product  $\chi_i = \bar{\chi} \prod_{\alpha} f_{\alpha}(\mathbf{x}_i; \{p_{\alpha}\}, \zeta_i)$ , where  $\bar{\chi}$ denotes the susceptibility of the metal, and each  $f_{\alpha}$  is a shape function characterized by geometric parameters  $\{p_{\alpha}\}$ . For improved convergence,  $f_{\alpha}$  also contains a smoothing kernel, allowing gradual variations between metal and non-metal regions. To obtain a binary structure, the  $\{\zeta_i\}$  smoothing parameters are reduced at each successive iteration of the optimization until the shape functions are piece-wise constant [91]. In what follows, this procedure, implemented with a simple 2d FDFD Maxwell solver [92], is applied to selectively enhance RHT at the thermal wavelength  $\lambda_{\rm opt} = 3 \ \mu {\rm m}$  corresponding to peak emission at T=1000 K. The surface–surface separation between the two bodies is fixed to be  $d = 0.02 \lambda_{\rm opt}$  (deeply in the sub wavelength regime).

We begin by considering tungsten gratings, which at  $\lambda_{\text{opt}}$ exhibits a highly metallic response  $\chi \approx -170 + 37i$  far from the planar SPP condition. Figure 1 depicts the spectral enhancement factor  $\mathcal{F}/\mathcal{F}_{\rm pl}^{2D}$  for both unstructured plates "(0)" and optimized gratings "(N)" obtained by successively increasing the number of (ellipsoidal) shapes allowed in each unit cell, N. The spectra of the two optimized gratings, illustrated as insets [93], both peak at  $\lambda_{opt}$  (black dashed line), with magnitudes  $\mathcal{F}/\mathcal{F}_{pl}^{2D}=\{0.40,0.53\}$  increasing with the number of ellipsoids,  $\{1,3\}[94]$ . On the one hand, enhancements of this magnitude for lossy metals,  $|\chi|/\mathrm{Im}(\chi) \gtrsim 1$ , are considered challenging [95] at small separations,  $d \ll \lambda_{\rm opt}$ . On the other hand, large RHT is known to be possible in ultra-thin films through the interference of coupled SPPs [96]. However, to reach the magnitudes obtained here, unrealistically small thicknesses  $\lesssim 1$  nm are needed. In contrast, no feature in the gratings of Fig. 1 is smaller than 10 nm. Notably, although the optimization is carried out at a single frequency, the discovered enhancement peaks are always broadband due to the high level of material absorption. Consequently, the frequency-integrated RHT at T = 1000 K exhibited by grating (3) is found to be roughly 10% larger than that of two

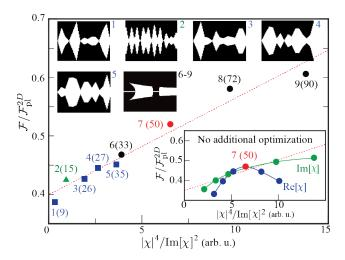


FIG. 2. Observation of material scaling in shape optimization: The figure highlights the material trend in enhancement  $\mathcal{F}/\mathcal{F}_{\mathrm{nl}}^{2D}$ found by optimizing grating geometries over a wide range of material susceptibilities  $\chi$ . Quantities displayed in parenthesis correspond to the relative enhancement of a given grating design compared to a planar geometry of the same material. Various shape parameterizations such as polylines, Fourier curves, and ellipsoids marked as squares, triangles, and circles are considered. The susceptibility values are chosen to vary along either the real or imaginary axis: gratings  $\{1, 2, 4\}$  correspond to  $\chi = \{-76, -101, -151\} + 50i$ , 5 to  $\chi = -151 + 40i$ ,  $\{3,7\}$  to  $\chi = \{-121, 169.5\} + 37.3i$ , and  $\{6\rightarrow9\}$  to  $\chi=-169.5+\{50,37.3,30,25\}i.$  Results for tungsten are colored red. The upper inset illustrates the unit cell of correspondingly numbered grating. (There is no visible difference for gratings 6-9 and so only one of these is shown.) The lower inset depicts the RHT of tungsten grating 7 when the susceptibility is varied without altering the structure. The dashed line represents the susceptibility scaling predicted by recently derived limits on RHT [34].

planar silicon carbide (black line), a low-loss polaritonic material. To explain this enhancement, Fig. 1 (right) examines the transfer function  $\mathcal{T}(\omega,k)$  versus frequency and wavenumber k. In moving from (1) to (3), the color plot demonstrates (frequency axis) that additional modes are successively created and pushed towards  $\omega_{\rm opt}$ , enhancing the density of states. Owing to the large size of the BZ (small periodicity  $\Lambda=0.04~\lambda_{\rm opt}$ ), we find that the range of rate matching achieved here is considerably larger than that observed in previously examined grating structures [68].

Another key finding is depicted in Fig 2, which plots RHT enhancement for representative optimizations [97] across an array of material and geometry combinations, as a function of the material scaling factor  $|\chi|^4/\text{Im}\left[\chi\right]^2$  of (1). Three different classes of design are explored: collections of ellipsoids (circles), single polyline interfaces (squares), and Fourier curves (triangles). Uniformly, every one of these structures is observed to enhance RHT by at least an order of magnitude compared to the corresponding planar systems and within factors of unity of the ideal planar bound, (3). Regardless of the particular parameterization, over the range of examined  $\text{Re}[\chi]$  and  $\text{Im}[\chi]$ , a clear linear trend in  $\mathcal{F}$  (red dotted line) as a function of  $|\chi|^4/\text{Im}[\chi|^2]$  is observed. This linear scal-

ing becomes increasingly difficult to observe at larger values of  $\chi$ , where larger resolutions are needed to accurately capture resonant behavior and the optimization requires increasingly larger number of iterations to find structures along the fit line. As should be expected, based on the fact that this behavior has not been previously reported, material scaling consistent with (1) is seen only for gratings optimized specifically for each particular value of  $\chi(\omega_{\mathrm{opt}})$ . For a fixed geometry, Fig. 2 (insets), varying either  $Re[\chi]$  or  $Im[\chi]$  shifts the resonance away from  $\omega_{\mathrm{opt}}$  and diminishes RHT. The appearance of this linear trend indicates that aspects of the arguments leading to the energy bounds in [34] are coming into play. However, the fact that a substantial increase in available design space has failed to significantly bridge the magnitude gap suggests that approaching these bounds (at least in 2d) may prove challenging with practical structures. Conversely, it should be emphasized that our results do not preclude the existence of structures with much larger enhancements. First, although the design space we have investigated is substantially larger than previous work, it is still relatively limited. Second, the complexity of the strutures and degree of enhancement are limited by the spatial resolution of the chosen discretization,  $0.0005 \lambda_{\text{opt}}$  (1/40th of the gap size).

To summarize, in investigating potential radiative heat transfer enhancements through inverse design, we have found evidence supporting the material scaling recently predicted by shape-indepedent bounds [34], a feature that to our knowledge had yet to be confirmed. While the observed heat transfer rates are still far from matching the magnitudes predicted by general bounds, we have found that RHT rates between fabricable tungsten gratings (a highly lossy metal), for subwavelength gap separations as small as 2% of the design wavelength, can selectively approach 50% of the rate achieved by ideal planar materials (lossless metals satisfying the SPP condition) in the infrared. The results represent nearly two orders of magnitude greater RHT rates in structured compared to planar materials. It remains to be seen to what degree similar strategies might enhance RHT in three dimensions, where the photonic density of states is larger and its associated dependence on material losses significantly stronger.

This work was supported by the National Science Foundation under Grant No. DMR-1454836, Grant No. DMR 1420541, and Award EFMA-1640986; and the National Science and Research Council of Canada under PDF-502958-2017.

## **Appendix A: Approximate Singular Value Decomposition**

In this appendix, we sketch how the low-rank nature of the RHT matrix  $\mathcal{Z}^{AB} = \sqrt{\text{Im}\left[\chi^A\right]}\mathcal{G}^{AB}\sqrt{\text{Im}\left[\chi^B\right]}$  entering (6) in the main text allows application of fast randomized singular value decompositions (SVD), greatly speeding up calculations of RHT. We begin by splitting the problem into two domains, referred to as bodies A and B, with associated superscripts denoting projection. It will be assumed that sources occur in body A and that the fields of interest lie only in body B. (From Lorentz reciprocity, the Green function must be symmetric under the exchange of observation and source po-

sitions, and so there is no loss of generality in either choice.) The algorithm, described in detail in [88], proceeds iteratively as follows.

Draw a random Gaussian distributed current vector  $\mathbf{j}_{i+1}$ with values in body A. Let  $\Omega_i^A$  denote the set of all previously drawn randomly Gaussian distributed current vectors (vertically concatenated to form a matrix). Solve Maxwell equation's to obtain the associated field,  $\mathbf{E}_{i+1} = \mathcal{G}\mathbf{j}_{i+1}$ . Let  $ilde{O}_i^{\scriptscriptstyle B}$  denote the set of all previously computed, orthonormalized, electromagnetic field vectors, and  $\tilde{Y}_i^B$  the set of all previous electromagnetic fields as originally calculated. Compute  $\tilde{\mathbf{o}}_{i+1}^{u_B} = \left(I - \tilde{O}_i^B \tilde{O}_i^{\dagger_B}\right) \tilde{\mathbf{E}}_{i+1}$ , and normalize the result  $\tilde{\mathbf{o}}_{i+1}^B = \tilde{\mathbf{o}}_{i+1}^{u_B} / \langle \tilde{\mathbf{o}}_{i+1}^{u_B} | \tilde{\mathbf{o}}_{i+1}^{u_B} \rangle$ , recording the value of  $\epsilon_{i+1} =$  $\langle \tilde{\mathbf{o}}_{i+1}^{u_B} | \tilde{\mathbf{o}}_{i+1}^{u_B} \rangle$ . Concatenate  $\tilde{\mathbf{o}}_{i+1}^{B}$  onto  $\tilde{O}_{i}^{B}$  and  $\tilde{\mathbf{E}}_{i+1}$  onto  $\tilde{Y}_{i}^{B}$ , producing  $\tilde{O}_{i+1}^{\scriptscriptstyle B}$  and  $\tilde{Y}_{i+1}^{\scriptscriptstyle B}$ . Similarly, draw random currents  $\tilde{\mathbf{j}}_{i+1}$  in body B and repeat the previous procedure, producing  $\tilde{O}_{i+1}^{\scriptscriptstyle A}$  and  $\tilde{Y}_{i+1}^{\scriptscriptstyle A}$ . The iterations are stopped when both  $\epsilon_{i+1}$ and  $\epsilon_{i+1}^{\dagger}$  (for both A and B calculations) are smaller than a prescribed singular value tolerance.

Given the above matrices, a low-rank approximation of the SVD of  $\mathcal{Z}^{AB}$  is obtained by expanding it onto the basis functions  $\tilde{O}^A$  and  $\tilde{O}^B$ . From random matrix theory [88], given that  $\epsilon_{i+1}$  is small for a given number of successive iterations, this basis approximately spans the domain and range of the matrix. It follows from Maxwell's equations that  $\tilde{Y}^A = \mathcal{G}^{AB}\tilde{\Omega}^B$  and hence.

$$\tilde{O}^{{\scriptscriptstyle A}\dagger} \mathcal{Z}^{{\scriptscriptstyle A}{\scriptscriptstyle B}} \tilde{O}^{{\scriptscriptstyle B}} \tilde{O}^{{\scriptscriptstyle B}} ^\dagger \sqrt{\mathrm{Im}[\chi^{\scriptscriptstyle B}]}^{-1} \tilde{\Omega}^{{\scriptscriptstyle B}} \approx \tilde{O}^{{\scriptscriptstyle A}\dagger} \sqrt{\mathrm{Im}[\chi^{\scriptscriptstyle A}]} \tilde{Y}^{{\scriptscriptstyle A}}.$$

Multiplication by the inverse of  $\tilde{O}^{B\dagger}\sqrt{\text{Im}[\chi^B]}^{-1}\tilde{\Omega}^B$  then produces a low-dimension  $k\times k$  matrix on the right hand side, amenable to standard SVD at minimal cost,

$$\tilde{O}^{A\dagger} \mathcal{Z}^{AB} \tilde{O}^{B} \approx \underbrace{\tilde{O}^{A\dagger} \sqrt{\operatorname{Im}[\chi_{A}]} \tilde{Y}^{A} \left( \tilde{O}^{B\dagger} \sqrt{\operatorname{Im}[\chi_{B}]}^{-1} \tilde{\Omega}^{B} \right)^{-1}}_{U\Sigma V^{\dagger}}.$$
(8)

The singular value approximation of  $\mathcal{Z}^{AB}$  is then derived from the small  $k \times k$  matrices  $U, \Sigma$ , and V,

$$\mathcal{Z}^{AB} \approx \tilde{O}^{A} U \Sigma V^{\dagger} \tilde{O}^{B\dagger}$$
$$= \left( \tilde{O}^{A} U \right) \Sigma \left( \tilde{O}^{B} V \right)^{\dagger} \tag{9}$$

Analysis of the convergence and performance properties of similar algorithms have been previously produced in [88].

## **Appendix B: Fast Gradient Adjoints**

To exploit gradient-based optimization, knowledge of  $\partial \Phi/(\partial p_{\alpha})$  is required for each optimization parameter  $p_{\alpha}$ . Letting  $\partial_{\alpha}$  denote a partial derivative with respect to  $p_{\alpha}$ , and retaining the notation of the main text and Appendix A,

$$\partial_{\alpha}\Phi = \frac{\omega^{4}\Theta}{2\pi c^{4}}\partial_{\alpha}\operatorname{Tr}\left[\operatorname{Im}\left[\chi^{B}\right]\mathcal{G}^{AB}^{\dagger}\operatorname{Im}\left[\chi^{A}\right]\mathcal{G}^{AB}\right].\tag{10}$$

Using the symmetry of  $\chi^A$  and  $\chi^B$ , along with the usual cyclic properties of the trace,

$$\begin{split} &\operatorname{Tr}\left[\operatorname{Im}\left[\chi^{B}\right]\partial_{\alpha}\mathcal{G}^{AB\dagger}\operatorname{Im}\left[\chi^{A}\right]\mathcal{G}^{AB}\right] = \\ &\operatorname{Tr}\left[\mathcal{G}^{AB\dagger}\operatorname{Im}\left[\chi^{A}\right]\partial_{\alpha}\mathcal{G}^{AB\ast}\operatorname{Im}\left[\chi^{B}\right]\right] = \\ &\operatorname{Tr}\left[\operatorname{Im}\left[\chi^{B}\right]\mathcal{G}^{AB\dagger}\operatorname{Im}\left[\chi^{A}\right]\partial_{\alpha}\mathcal{G}^{AB\ast}\right], \end{split}$$

one finds that the second and fourth terms in the partial derivative expansion are complex conjugates. (Here,  $\uparrow$  denotes transposition without complex conjugation.) Given that  $\mathcal{G} = \left[ (\nabla \times \nabla \times) - \omega^2 \epsilon \right]^{-1}$  is the inverse Maxwell operator,

$$\partial_{\alpha} \mathcal{G}^{AB} = \omega^2 \, \mathcal{G}^{A} \partial_{\alpha} \chi \, \mathcal{G}^{B}$$

and so one finds:

$$\partial_{\alpha} \Phi = \frac{\omega^{4} \Theta}{2\pi c^{4}} \operatorname{Tr} \left[ \mathcal{G}^{AB\dagger} \operatorname{Im} \left[ \chi^{A} \right] \mathcal{G}^{AB} \operatorname{Im} \left[ \partial_{\alpha} \chi^{B} \right] + \right.$$

$$\mathcal{G}^{AB} \operatorname{Im} \left[ \chi^{B} \right] \mathcal{G}^{AB\dagger} \operatorname{Im} \left[ \partial_{\alpha} \chi^{A} \right] +$$

$$2\omega^{2} \operatorname{Re} \left[ \mathcal{G}^{B} \operatorname{Im} \left[ \chi^{B} \right] \mathcal{G}^{AB\dagger} \operatorname{Im} \left[ \chi^{A} \right] \mathcal{G}^{AB} \partial_{\alpha} \chi \right] \right].$$

$$(11)$$

The  $\mathcal{G}^{AB}$  matrices involved in (11) are low rank, and can computed alongside  $\mathcal{Z}^{AB}$  at almost no extra cost. Specifically, if  $\sqrt{\operatorname{Im}\left[\chi^{A}\right]}$  and  $\sqrt{\operatorname{Im}\left[\chi^{B}\right]}$  are excluded from the error estimates  $\epsilon_{i+1}$  and  $\epsilon_{i+1}^{\dagger}$ , one obtains an approximation for  $\mathcal{G}^{BA}$  rather than  $\mathcal{Z}^{AB}$ . Both computations can be carried out at the same time, using the same current sources and field solutions. If these matrices have rank k, the parameter independent matrices of (11) are solved in order k computations. Hence, determination of the gradient is essentially no more costly than the determination of  $\Phi$ .

- A. Kittel, W. Müller-Hirsch, J. Parisi, S.-A. Biehs, D. Reddig, and M. Holthaus, Physical Review Letters 95, 224301 (2005).
- [2] K. Kim, B. Song, V. Fernández-Hurtado, W. Lee, W. Jeong, L. Cui, D. Thompson, J. Feist, M. H. Reid, F. J. García-Vidal, et al., Nature 528, 387 (2015).
- [3] B. Song, Y. Ganjeh, S. Sadat, D. Thompson, A. Fiorino, V. Fernández-Hurtado, J. Feist, F. J. Garcia-Vidal, J. C. Cuevas, P. Reddy, *et al.*, Nature Nanotechnology 10, 253 (2015).
- [4] R. St-Gelais, L. Zhu, S. Fan, and M. Lipson, Nature Nanotechnology 11, 515 (2016).
- [5] J. Pendry, Journal of Physics: Condensed Matter 11, 6621 (1999).
- [6] R. Carminati and J.-J. Greffet, Physical Review Letters 82, 1660 (1999).
- [7] A. Volokitin and B. Persson, Physical Review B 63, 205404 (2001).
- [8] A. Babuty, K. Joulain, P.-O. Chapuis, J.-J. Greffet, and Y. De Wilde, Physical Review Letters 110, 146103 (2013).
- [9] A. Narayanaswamy and G. Chen, Applied Physics Letters 82, 3544 (2003).
- [10] M. Laroche, R. Carminati, and J.-J. Greffet, Journal of Applied Physics 100, 063704 (2006).

- [11] K. Park, S. Basu, W. P. King, and Z. Zhang, Journal of Quantitative Spectroscopy and Radiative Transfer 109, 305 (2008).
- [12] O. Ilic, M. Jablan, J. D. Joannopoulos, I. Celanovic, and M. Soljačić, Optics Express 20, A366 (2012).
- [13] A. Karalis and J. Joannopoulos, Scientific Reports 7, 14046 (2017).
- [14] R. St-Gelais, G. R. Bhatt, L. Zhu, S. Fan, and M. Lipson, ACS Nano 11, 3001 (2017).
- [15] B. Guha, C. Otey, C. B. Poitras, S. Fan, and M. Lipson, Nano Letters 12, 4546 (2012).
- [16] Y. Yang, S. Basu, and L. Wang, Applied Physics Letters 103, 163101 (2013).
- [17] C. Khandekar, R. Messina, and A. W. Rodriguez, AIP Advances 8, 055029 (2018).
- [18] W. Challener, C. Peng, A. Itagi, D. Karns, W. Peng, Y. Peng, X. Yang, X. Zhu, N. Gokemeijer, Y.-T. Hsia, *et al.*, Nature Photonics 3, 220 (2009).
- [19] S. Bhargava and E. Yablonovitch, IEEE Transactions on Magnetics 51, 3100407 (2015).
- [20] A. Volokitin and B. N. Persson, Rev. Mod. Phys. 79, 1291 (2007).
- [21] H. Iizuka and S. Fan, Physical Review B 92, 144307 (2015).
- [22] G. Domoto, R. Boehm, and C. L. Tien, Journal of Heat Transfer 92, 412 (1970).
- [23] T. Kralik, P. Hanzelka, M. Zobac, V. Musilova, T. Fort, and M. Horak, Physical Review Letters 109, 224302 (2012).
- [24] T. Ijiro and N. Yamada, Applied Physics Letters 106, 023103 (2015).
- [25] S. Lang, G. Sharma, S. Molesky, P. U. Kränzien, T. Jalas, Z. Jacob, A. Y. Petrov, and M. Eich, Scientific Reports 7, 13916 (2017).
- [26] S. Shen, A. Narayanaswamy, and G. Chen, Nano Letters 9, 2909 (2009).
- [27] T. Luo and G. Chen, Physical Chemistry Chemical Physics 15, 3389 (2013).
- [28] S. Basu, Y.-B. Chen, and Z. Zhang, International Journal of Energy Research 31, 689 (2007).
- [29] E. Rephaeli and S. Fan, Optics Express 17, 15145 (2009).
- [30] S. Molesky, C. J. Dewalt, and Z. Jacob, Optics Express 21, A96 (2013).
- [31] P. Nagpal, D. P. Josephson, N. R. Denny, J. DeWilde, D. J. Norris, and A. Stein, Journal of Materials Chemistry 21, 10836 (2011).
- [32] V. Rinnerbauer, Y. X. Yeng, W. R. Chan, J. J. Senkevich, J. D. Joannopoulos, M. Soljačić, and I. Celanovic, Optics Express 21, 11482 (2013).
- [33] P. Dyachenko, S. Molesky, A. Y. Petrov, M. Störmer, T. Krekeler, S. Lang, M. Ritter, Z. Jacob, and M. Eich, Nature Communications 7 (2016).
- [34] O. D. Miller, S. G. Johnson, and A. W. Rodriguez, Physical Review Letters 115, 204302 (2015).
- [35] V. Fernández-Hurtado, F. J. Garcia-Vidal, S. Fan, and J. C. Cuevas, Physical Review Letters 118, 203901 (2017).
- [36] J. Dai, F. Ding, S. I. Bozhevolnyi, and M. Yan, Physical Review B 95, 245405 (2017).
- [37] R. Guérout, J. Lussange, F. Rosa, J.-P. Hugonin, D. Dalvit, J.-J. Greffet, A. Lambrecht, and S. Reynaud, in *Journal of Physics: Conference Series*, Vol. 395 (IOP Publishing, 2012) p. 012154.
- [38] J. Lussange, R. Guérout, F. S. Rosa, J.-J. Greffet, A. Lambrecht, and S. Reynaud, Physical Review B 86, 085432 (2012).
- [39] B. Liu and S. Shen, Physical Review B 87, 115403 (2013).
- [40] W. Jin, R. Messina, and A. W. Rodriguez, Optics Express 25, 293277 (2017).
- [41] S. Molesky, Z. Lin, A. Y. Piggott, W. Jin, J. Vuckovic, and

- A. W. Rodriguez, arXiv:1801.06715 (2018).
- [42] M. Pralle, N. Moelders, M. McNeal, I. Puscasu, A. Greenwald, J. Daly, E. Johnson, T. George, D. Choi, I. El-Kady, et al., Applied Physics Letters 81, 4685 (2002).
- [43] M. De Zoysa, T. Asano, K. Mochizuki, A. Oskooi, T. Inoue, and S. Noda, Nature Photonics 6, 535 (2012).
- [44] N. Liu, M. Mesch, T. Weiss, M. Hentschel, and H. Giessen, Nano Letters 10, 2342 (2010).
- [45] A. W. Rodriguez, O. Ilic, P. Bermel, I. Celanovic, J. D. Joannopoulos, M. Soljačić, and S. G. Johnson, Physical Review Letters 107, 114302 (2011).
- [46] A. W. Rodriguez, M. H. Reid, and S. G. Johnson, Physical Review B 86, 220302 (2012).
- [47] C. R. Otey, L. Zhu, S. Sandhu, and S. Fan, Journal of Quantitative Spectroscopy and Radiative Transfer **132**, 3 (2014).
- [48] R. Messina, A. Noto, B. Guizal, and M. Antezza, Physical Review B 95, 125404 (2017).
- [49] S. Boyd and L. Vandenberghe, Convex Optimization (Cambridge University Press, 2004).
- [50] S. Edalatpour and M. Francoeur, Physical Review B 94, 045406 (2016).
- [51] X. Liu, L. Wang, and Z. M. Zhang, Nanoscale and Microscale Thermophysical Engineering 19, 98 (2015).
- [52] S.-A. Biehs, P. Ben-Abdallah, F. S. Rosa, K. Joulain, and J.-J. Greffet, Optics Express 19, A1088 (2011).
- [53] Y. Guo, C. L. Cortes, S. Molesky, and Z. Jacob, Applied Physics Letters 101, 131106 (2012).
- [54] X. Liu, R. Zhang, and Z. Zhang, Applied Physics Letters 103, 213102 (2013).
- [55] X. Liu, R. Zhang, and Z. Zhang, International Journal of Heat and Mass Transfer 73, 389 (2014).
- [56] J. Shi, B. Liu, P. Li, L. Y. Ng, and S. Shen, Nano Letters 15, 1217 (2015).
- [57] A. Didari and M. P. Mengüç, Optics Express 23, A1253 (2015).
- [58] P. Ben-Abdallah, K. Joulain, J. Drevillon, and G. Domingues, Journal of Applied Physics 106, 044306 (2009).
- [59] M. Francoeur, M. P. Mengüç, and R. Vaillon, Journal of Physics D: Applied Physics 43, 075501 (2010).
- [60] S. Basu and M. Francoeur, Applied Physics Letters 98, 243120 (2011).
- [61] P. Van Zwol, K. Joulain, P. Ben-Abdallah, and J. Chevrier, Physical Review B 84, 161413 (2011).
- [62] S. Pendharker, H. Hu, S. Molesky, R. Starko-Bowes, Z. Poursoti, S. Pramanik, N. Nazemifard, R. Fedosejevs, T. Thundat, and Z. Jacob, Journal of Optics 19, 055101 (2017).
- [63] G. V. Naik, V. M. Shalaev, and A. Boltasseva, Advanced Materials 25, 3264 (2013).
- [64] H. Chalabi, A. Alù, and M. L. Brongersma, Physical Review B 94, 094307 (2016).
- [65] X. Liu and Z. Zhang, ACS Photonics 2, 1320 (2015).
- [66] Z. Zheng, A. Wang, and Y. Xuan, Journal of Quantitative Spectroscopy and Radiative Transfer (2018).
- [67] X. L. Liu and Z. M. Zhang, Applied Physics Letters 104, 251911 (2014).
- [68] J. Dai, S. A. Dyakov, and M. Yan, Physical Review B 92, 035419 (2015).
- [69] X. Liu, B. Zhao, and Z. M. Zhang, Phys. Rev. A 91, 062510 (2015).
- [70] There is a considerable body of work in this area. The accuracy of effective medium approximations has been explored for both one- and two-dimensional grating structures, with and without dielectric filling [? ?].
- [71] E. Prodan, C. Radloff, N. J. Halas, and P. Nordlander, science 302, 419 (2003).

- [72] S.-A. Biehs, E. Rousseau, and J.-J. Greffet, Physical Review Letters 105, 234301 (2010).
- [73] H. Chalabi, E. Hasman, and M. L. Brongersma, Physical Review B 91, 174304 (2015).
- [74] C. L. Baldwin, N. W. Bigelow, and D. J. Masiello, Journal of Physical Chemistry Letters 5, 1347 (2014).
- [75] J. E. Pérez-Rodríguez, G. Pirruccio, and R. Esquivel-Sirvent, Physical Review Materials 1, 062201 (2017).
- [76] S. Molesky and Z. Jacob, Physical Review B 91, 205435 (2015).
- [77] B. Liu, J. Li, and S. Shen, ACS Photonics (2017).
- [78] P. Wang and R. Menon, Optics Express 22, A99 (2013).
- [79] V. Ganapati, O. D. Miller, and E. Yablonovitch, IEEE Journal of Photovoltaics 4, 175 (2014).
- [80] M. Diem, T. Koschny, and C. M. Soukoulis, Physical Review B 79, 033101 (2009).
- [81] M. K. Hedayati, M. Javaherirahim, B. Mozooni, R. Abdelaziz, A. Tavassolizadeh, V. S. K. Chakravadhanula, V. Zaporojtchenko, T. Strunkus, F. Faupel, and M. Elbahri, Advanced Materials 23, 5410 (2011).
- [82] D. M. Nguyen, D. Lee, and J. Rho, Scientific Reports 7, 2611 (2017).
- [83] S. M. Rytov, Y. A. Kravtsov, and V. I. Tatarskii, (1988).
- [84] J. A. Kong, New York, Wiley-Interscience, 1975. 348 p. (1975).
- [85] X. S. Li and J. W. Demmel, ACM Transactions on Mathemati-

- cal Software (TOMS) 29, 110 (2003).
- [86] R.-E. Plessix, Geophysics 72, SM185 (2007).
- [87] P. Gatto and J. S. Hesthaven, arXiv preprint arXiv:1508.07798 (2015).
- [88] N. Halko, P.-G. Martinsson, and J. A. Tropp, SIAM review 53, 217 (2011).
- [89] J. Caers and T. Hoffman, Mathematical Geology 38, 81 (2006).
- [90] R. Martinez-Cantin, The Journal of Machine Learning Research 15, 3735 (2014).
- [91] Y. Tsuji and K. Hirayama, IEEE photonics technology letters 20, 982 (2008).
- [92] F. Xu, Y. Zhang, W. Hong, K. Wu, and T. J. Cui, IEEE Transactions on Microwave Theory and Techniques **51**, 2221 (2003).
- [93] Full geometric characterizations of these structures and those presented later in the text are available upon request.
- [94] The optimizations involving four elliptical bodies usually require  $\approx 10^2$  iterations to reach convergence; roughly 200 hours of total computation time for each structure.
- [95] H. Raether, in Surface plasmons on smooth and rough surfaces and on gratings (Springer, 1988) pp. 91–116.
- [96] Y. Guo, S. Molesky, H. Hu, C. L. Cortes, and Z. Jacob, Applied Physics Letters 105, 073903 (2014).
- [97] The structures with the best performance features over all trials with the same susceptibility.